High-Performance Quality Factor Based Sensor With Diagonal Cylinder Metasurface of the Bound State in the Continuum

Yuxuan CHEN[1], Yuke LI[1], Zhengda HU[1], Zexiang WANG[1], Zhenxing LI[1], and Jicheng WANG[1,2*]

[1]*School of Science, Jiangsu Provincial Research Center of Light Industrial Optoelectronic Engineering and Technology, Jiangnan University, Wuxi 214122, China*

[2]*State Key Laboratory of Millimeter Waves, Southeast University, Nanjing 210096, China*

[*]Corresponding author: Jicheng WANG E-mail: jcwang@jiangnan.edu.cn

Abstract: High-quality-factor (high-*Q*-factor) electromagnetic resonance plays an important role in sensor applications. Previously proposed gas refractive index sensors are often limited by the large cavity length or microscale fabrication process in practical applications. Recently, ultra-high *Q* factor resonance based on the bound state in the continuum (BIC) has provided a feasible approach to solve these problems. In this paper, we propose a metasurface structure consisting of a single size tetramer cylinder. It supports dual band toroidal dipole (TD) resonances driven by BIC. The physical mechanism of double TD resonances is clarified by the multipole decomposition of the metasurface band structure and far-field scattering power. The sensor structure based on this achieves a sensitivity of 518.3 MHz/RIU, and the maximum line width does not exceed 680 kHz. The high-*Q*-factor electromagnetic resonance has the advantages of polarization independence and simplicity to manufacture. These findings will open up an avenue to develop the ultrasensitive sensor in the gigahertz regime.

Keywords: Metasurfaces; bound state in the continuum; toroidal dipole

Citation: Yuxuan CHEN, Yuke LI, Zhengda HU, Zexiang WANG, Zhenxing LI, and Jicheng WANG, "High-Performance Quality Factor Based Sensor With Diagonal Cylinder Metasurface of the Bound State in the Continuum," *Photonic Sensors*, 2023, 13(2): 230332.

1. Introduction

As high-*Q* resonance has wide prospects in many fields, including narrowband filtering [1], microwave and optical filters, thin-film sensing [2], and guided-Mode resonant gratings [3]. The high-*Q* resonance based on high-index dielectric nanoparticles [4], electromagnetic induction transparency (EIT) [5], and surface plasmon polaritons (SPPs) [6] has been reported in previous studies. Recently, a class of asymmetric metasurfaces with high-*Q* resonance based on the bound states in the continuum (BIC) phenomenon has attracted wide attention. The high-*Q* resonance driven by quasi-BIC is sensitive to the background refractive index, which is very convenient for designing ultra-sensitive refractive index sensors. Maksimov's work has proved that the refractive index sensing with optical bounds states in the continuum can be implemented in dielectric structures [7]. The feasibility of good performance of refractive index sensors driven by BIC in experiments has also been demonstrated in recent work [8].

Received: 17 May 2022 / Revised: 9 September 2022

DOI: 10.1007/s13320-022-0673-6
Article type: Regular

BIC was first proposed by von Neumann and Wigner in 1929 as a concept of quantum domain to describe the isolated eigenvalues of single-particle Schrödinger equations embedded in the continuum of positive energy states [9]. It has been observed in experiments of electromagnetic, acoustic, and water waves [10]. A true BIC with disappeared resonance linewidths and infinite-Q factors can exist only in ideal lossless infinite structures or extreme values of parameters [11], so it cannot be observed in the electromagnetic spectrum. Symmetry-protected BICs exist in periodic structures, which can be understood as the bound states of one symmetric class embedded in the continuum spectrum of another symmetric class. While the symmetry of the system is preserved, their coupling is forbidden. Therefore, by breaking the symmetry of the system, the bound state turns into a leaky resonance. In this way, BIC is transformed into quasi-BIC and Q becomes limited but very high.

In this paper, we demonstrate that dual-band resonances can be induced in a metasurface structure with a periodic array of tetramer cylinders. The excitation of the double modes is realized by the symmetry breaking of the tetramer cylinders superlattice. Dual-band resonances are driven by quasi-BIC and displayed in the band structure of the metasurface. Far-field multipole decompositions and near-field distributions of the metasurface prove that the resonances are caused by toroidal dipole. And these low-loss toroidal dipole (TD) resonances with the extremely narrow linewidth are very sensitive to changes in the refractive index of the surrounding medium. The dual-band resonances can be still maintained with the change of the geometrical parameters. Benefiting from these characteristics of the metasurface, we design an ultra-sensitive gas refractive index sensor based on this structure. This symmetric periodic structure of the sensor can excite a small number of modes while still maintaining the C_4 symmetry, making it polarization independent. Its sensitivity reaches 518.3 MHz/RIU and figure of merit (FoM) reaches 2160. This proves a feasible approach for the development of GHz sensors.

2. Analysis of metasurface structure and its band structure

Figure 1(a) illustrates the schematic of the metasurface structure. Four aluminum oxide cylinders with the same size on a quartz glass substrate serve as a structural unit of the metasurface. The lattice constant is a=20 mm, the height of the quartz glass substrate is h_1=10 mm, the cylinder radius is R=22 mm, and the cylinder height is h_0= 5 mm. A top view of the unit cell in the x-y plane is shown in Fig. 1(b). When the metasurface is symmetry-protected, each cylinder is in the center of a quarter of the lattice. The asymmetric parameter $P=P_x=P_y$ represents the axial displacement of the cylinder shrinking (P>0) or expanding (P<0) from the symmetry-protected position to the center of the cell. For $P\neq0$, it means the introduction of symmetry breaking. The reflection spectrum of the metasurface presented in this paper is calculated by using the finite element method commercial software of COMSOL Multiphysics. Periodic boundary conditions are set in both x and y directions, and perfect matching layers are set at the upper and lower parts of the unit cell. The calculation results are shown in Fig. 2. There is no resonance for the symmetry-protected matesurface with P=0 mm. When the axial displacement parameters P of the metasurface is set to 0.5 mm, the resonance of total reflection can be observed at 7.931 1 GHz and 9.1184 GHz.

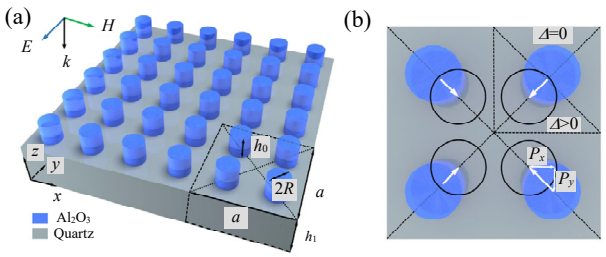

Fig. 1 Schematic of the all-dielectric metasurface structure: (a) 3D schematic of the GHz all-dielectric metasurface structure and (b) top view (x-y plane) of the unit cell.

Figure 2(c) shows the dispersion curves for transverse electric (TE)-like modes and transverse magnetic (TM)-like modes along *X*-*Γ*-*X*′. The solid black line represents TE-like mode, and the dotted blue line represents TM-like mode. The labeled numbers represent the indexes of the corresponding bands, and the figure on the right corresponds to their electromagnetic field distributions at points *Γ* in *k*-space, which helps us to understand the nature of BIC. These eigenmodes can be divided into two types: modes whose distributions of electromagnetic fields are even (Modes 1, 3, and 5) and modes whose distributions of electromagnetic fields which are odd (Modes 2 and 4) under C_4.

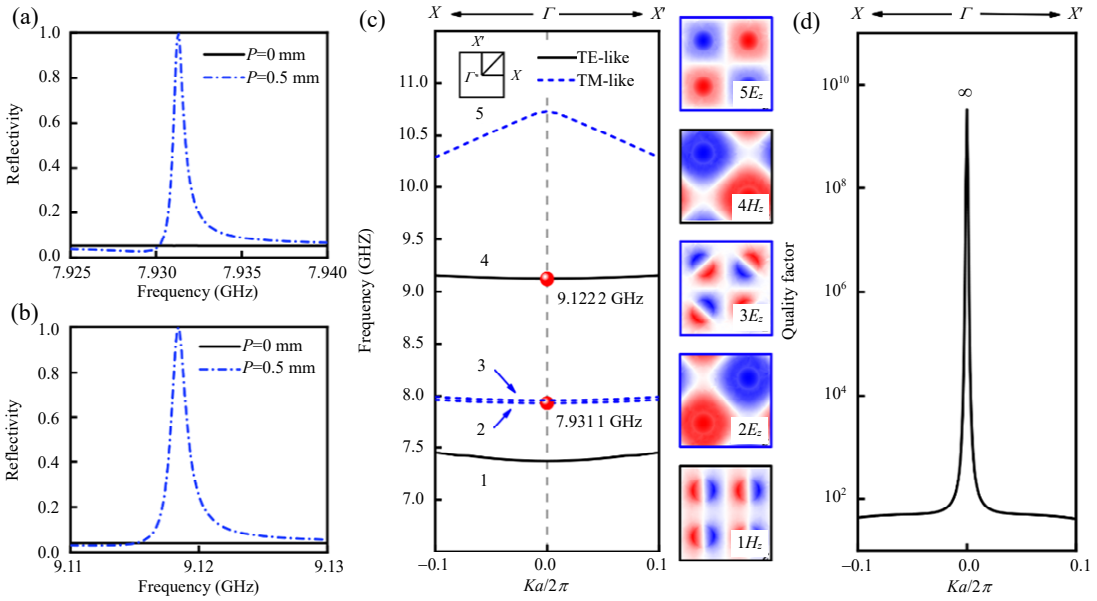

Fig. 2 Reflection spectra of modes at the metasurface: (a) reflection spectra of Mode 1 at symmetric (*P*=0 mm) and asymmetric (*P*=0.5 mm) metasurfaces, (b) reflection spectra of Mode 2 at symmetric (*P*=0 mm) and asymmetric (*P*=0.5 mm) metasurfaces, (c) band diagrams along *X*-*Γ*-*X*′ (*ka*/2*π*) of the metasurface. The out-of-plane components of their electromagnetic fields are shown in the right panel, and (d) quality factor distribution corresponding to the BIC band.

At frequencies below the diffraction limit $\omega c = 2na$ [10], the only radiating channel at the *Γ* point is a plane wave along the *z* axis [12]. So, the electromagnetic field distribution of a normal incident plane wave with any linear polarization direction is odd with respect to the C_4 symmetry around the *z* axis. While the electromagnetic field distributions that are even cannot be excited at the *Γ* point due to the mode symmetry mismatch. Therefore, in this paper, Modes 1 and 3 can be excited by the normal incident plane wave with $E_y(E_x)$ polarization. At the same time, the mode with even electromagnetic field distribution will be prohibited, which avoids the interference of multiple modes excitation for ultrasensitive sensing applications. When a transmission electron microscope (TEM) wave is incident, there are only two resonances in the corresponding frequency band. And the intrinsic frequencies corresponding to Modes 1 and 2 are respectively consistent with the two resonant frequencies of the metasurface with symmetric breaking, which confirms the previous analysis.

We also calculate that the quality factors of these eigenmodes are odd. The quality factor is defined as the ratio of the real part (ω_0) and imaginary part (γ) of the intrinsic frequency, i.e., $Q=\omega_0/2\gamma$, and γ is related to the radiation loss. The calculation result of Band 2 is shown in Fig. 2(d). It can be seen that the quality factor approaches infinity when the dispersion curve approaches the point *Γ* in the *k*-space. When the metasurface is at the *Γ* point, the coupling of certain resonances to the radiation modes are forbidden by symmetry. And when it deviates slightly from the BIC point, it will show radiation to the outside of the metasurface [13].

3. Properties of metasurface

Figure 3 shows the electromagnetic field distribution corresponding to the peak frequencies of the two modes of the metasurface to explore the origin of resonance. The red cones represent the displacement current density, and the blue cones represent the magnetic field vector. For Mode 1, as shown in Figs. 3(a) and 3(c), the displacement current vector forms a loop between adjacent cylinders in the *x*-*z* plane, and the induced magnetic field vector in the *y* direction forms a closed magnetic vortex in each alumina cylinder, which is a characterization of the TD resonance. And the direction of the TD is along the *z* direction according to the right-hand screw rule. For Mode 2, the displacement currents circulation direction of adjacent cylinders in the *y* direction is opposite and the displacement current circulation direction of adjacent cylinders in the *x* direction is the same, which indicates that an opposite-phase magnetic dipole along the *z* direction is induced in the cylinder pair in the *y* direction. The magnetic field vector circulates counterclockwise between adjacent cylinders in the *y*-*z* plane, producing TD in the *x* direction. More importantly, the electric field of the TD mode concentrates on the metasurface and the surrounding air layer. In this case, more analytes will be covered by electric fields in the TD mode, achieving better spatial overlap and stronger light-matter interactions [14].

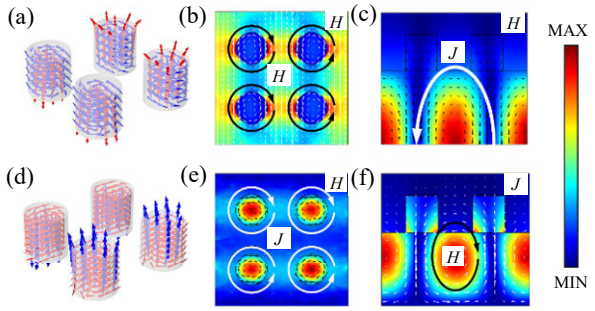

Fig. 3 Electromagnetic field distribution of two modes: (a) and (d) orientation of displacement current (red cones) and magnetic field vector (blue cones) is within the structural units of two modes; (b) and (e) electromagnetic field distribution of two modes in the *x*-*y* plane (*z* is half height of cylinder); (c) and (f) electromagnetic field distribution of two modes in the *x*-*z* plane and *x*-*z* plane, respectively. The black arrow represents the magnetic field vector, and the white arrow represents the displacement current.

To prove that the two resonant modes in our proposed structure are related to a toroidal dipolar mode, we carry out multipole decomposition of displacement currents in terms of five strongest multipoles: electric dipolar moment (ED) **P**, magnetic dipolar moment (MD) **M**, electric quadrupole moment (EQ) $\mathbf{Q}^{(e)}_{\alpha,\beta}$, magnetic quadrupole moment (MQ) $\mathbf{Q}^{(m)}_{\alpha,\beta}$, and toroidal dipolar moment (TD) **T**, respectively. The multipole moments can be calculated based on the displacement current density **j** [15, 16]:

$$\mathbf{P}=\frac{1}{\mathrm{i}\omega}\int \mathbf{j}\mathrm{d}^3r \tag{1}$$

$$\mathbf{M}=\frac{1}{10c}\int(\mathbf{r}\times\mathbf{j})\mathrm{d}^3r \tag{2}$$

$$\mathbf{T}=\frac{1}{10c}\int\left[(\mathbf{r}\cdot\mathbf{j})\mathbf{r}-2r^2\mathbf{j}\right]\mathrm{d}^3r \tag{3}$$

$$\mathbf{Q}^{(e)}_{\alpha,\beta}=\frac{1}{2\mathrm{i}\omega}\int\left[(r_\alpha j_\beta+r_\beta j_\alpha)-\frac{2}{3}(\mathbf{r}\cdot\mathbf{j})\delta_{\alpha,\beta}\right]\mathrm{d}^3r \tag{4}$$

$$\mathbf{Q}^{(m)}_{\alpha,\beta}=\frac{1}{3c}\int\left[(\mathbf{r}\times\mathbf{j})_\alpha r_\beta+(\mathbf{r}\times\mathbf{j})_\beta r_\alpha\right]\mathrm{d}^3r \tag{5}$$

where **r** is the position vector, ω is the frequency of incident light, c is the light speed in vacuum, and α, $\beta=x, y, z$. Here the charge density ρ, which usually appears in the definition of ED and MQ, has been replaced with displacement current density **j** via charge conservation relationship of $\mathrm{i}\omega\rho+\nabla\cdot\mathbf{j}=0$ [17]. In the case of harmonic excitation $\sim\exp(\mathrm{i}\omega t)$ the expression of the far-field radiated power for different multipoles has the form [18]:

$$\begin{aligned}I=&\frac{2\omega^4}{3c^3}|\mathbf{P}|^2+\frac{2\omega^4}{3c^3}|\mathbf{M}|^2+\\&\frac{2\omega^6}{3c^5}|\mathbf{T}|^2+\frac{\omega^6}{5c^5}\sum_{\alpha,\beta}|\mathbf{Q}^{(e)}_{\alpha,\beta}|^2+\\&\frac{\omega^6}{20c^5}\sum_{\alpha,\beta}|\mathbf{Q}^{(m)}_{\alpha,\beta}|^2+o\left(\frac{1}{c^5}\right)\end{aligned} \tag{6}$$

where the five terms correspond to ED, MD, TD, EQ, and MQ. The last term is a higher-order term, which contains the high-order multipole scattering and coupling between them, which can be generally ignored [19].

Refer to (1)–(6), the contribution of different

multipoles to far-field scattering power can be obtained. The calculation results are shown in Fig. 4. It can be clearly seen in Figs. 4(a) and 4(c) that, for the metasurface P=0, only MD has weak resonance in the frequency band near the BIC point, and the other components do not fluctuate significantly in the frequency region of interest. In the case of $P\neq0$, dual-band resonances are realized as BICs are transformed to quasi-BICs because of the symmetry breaking of the metasurface, i.e., from the centrosymmetry of simple lattice to the four-fold symmetry (C_4) of superlattice. When we set the geometric displacement parameter P to 0.5 mm, the scattered power from toroidal dipolar moment TD is significantly enhanced at each frequency position matching the reflection peaks in Figs. 2(a) and 2(b). And TD plays a dominant role in both resonant modes, which clearly indicates that the resonant modes of the two modes are closely related to the excitation of the toroidal dipole mode.

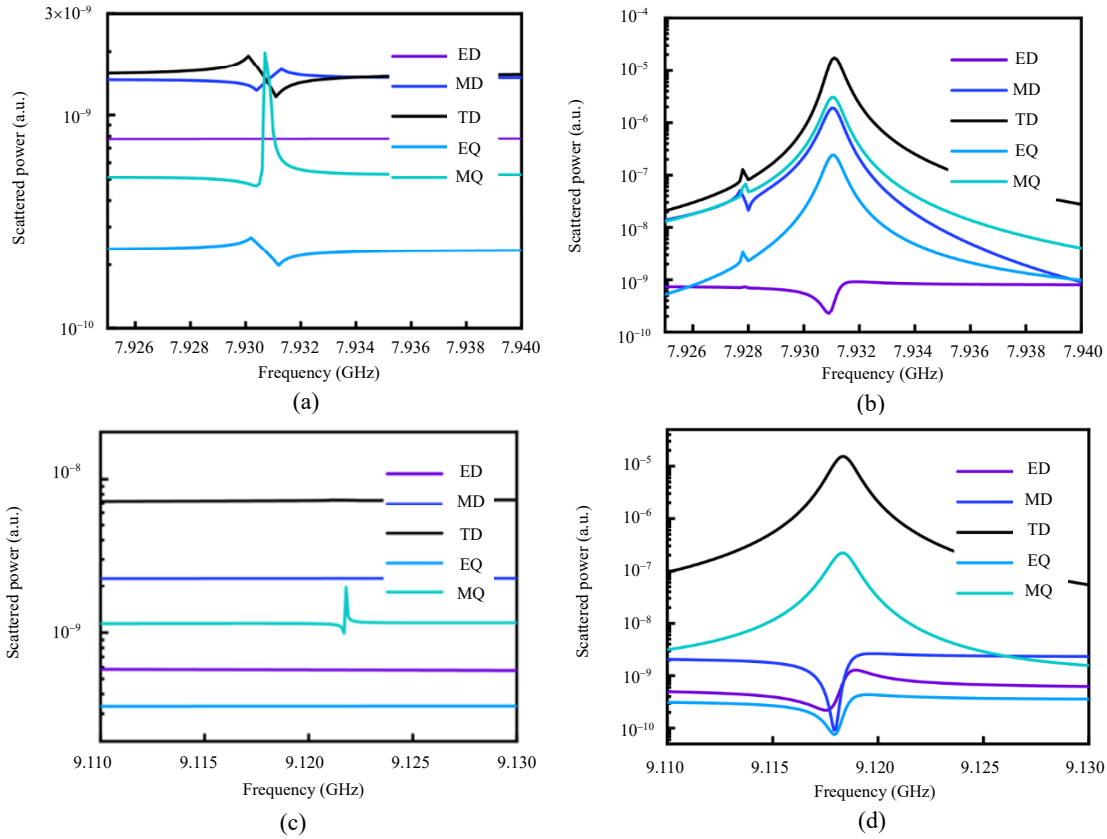

Fig. 4 Multipole decomposition of modes: (a) and (b) multipole decomposition of Mode 1 (P=0 and P=0.5 mm); (c) and (d) multipole decomposition of Mode 2 (P=0 and P=0.5 mm).

4. Geometric properties of metasurface

In Fig. 2, we observe that the intrinsic frequencies corresponding to the two BIC points do not exactly match the peak positions of the two modes. Figures 5(a) and 5(d) show the relationship between the resonant frequencies of the two modes and the asymmetric parameter P. With the increase of P, the line width increases, and the resonant frequency of Mode 2 moves to the short-wave direction, while the resonance frequency of Mode 1 hardly changes. This means that we can adjust the line width and resonance frequency of Mode 1 by adjusting P and other geometric parameters, respectively. For an asymmetric metasurface structure, we calculate the corresponding Q factors of Modes 1 and 2 at different asymmetric parameters P. We use the following formula to calculate the Q factor:

$$Q=\frac{f_0}{\mathrm{FWHM}} \tag{7}$$

where f_0 is the frequency of the resonance, and FWHM is the half band width of the reflection peak. Figures 5(c) and 5(d) shows the relationship between the asymmetric parameter P and the Q factor for Modes 1 and 2, respectively. They show symmetry with respect to the position P=0, which indicates that for P with the same absolute value, the Q factor of the corresponding mode is almost the same, because when the tetramer cylinders are shrunk or expanded along the diagonals of the unit cell, the C_4 symmetry of metasurface is still maintained. The relationship of the Q factor on P of both modes subject to the inverse quadratic law, i.e., $Q \propto P^{-2}$, which is consistent with what has been suggested in [20]. The Q factor for Mode 1 increases to an ultrahigh value of 2.4×10^6 as $|P|$ approaches to 0 mm and become infinite at P=0 mm. The Q factor of Mode 2 has a similar variation trend as that of Mode 1 and reaches an ultrahigh value of 4.9×10^6 near P=0 mm and achieves the infinity factor at P=0 mm. As shown in Figs. 1(a) and 1(b), when P=0, the symmetry-protected BIC cannot be excited by normal incident plane waves, the Q factors approaches infinity, and the resonance linewidth vanishes.

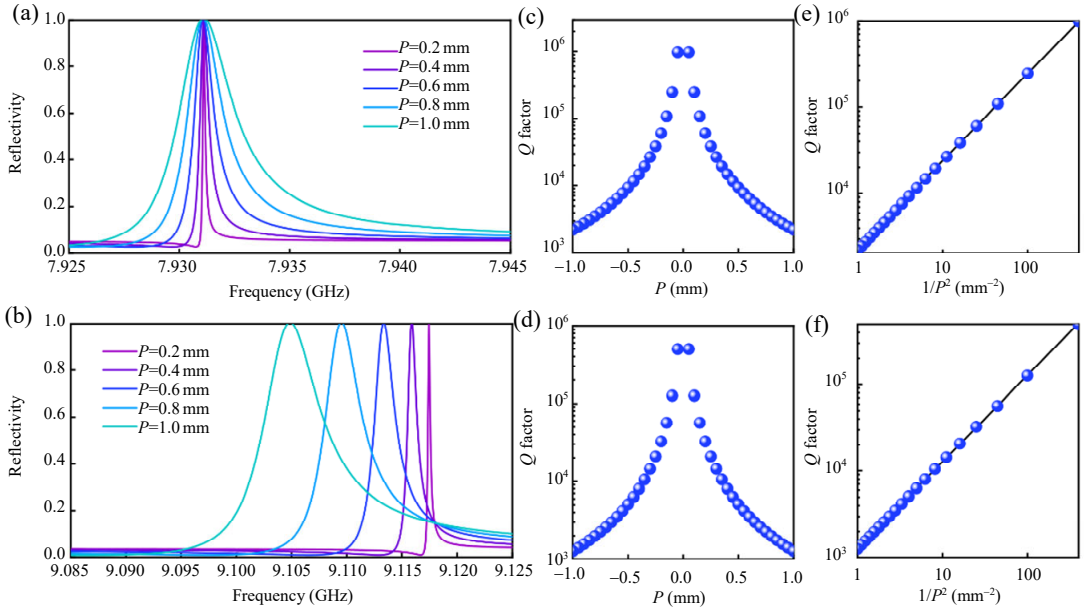

Fig. 5 Reflection spectrum and Q factor when asymmetric parameters change: (a)–(c) Mode 1 and (d)–(f) Mode 2.

To investigate the dependence of dual modes resonant frequencies on the geometric parameters of the metasurface, we calculate the change of transmission response due to fine-tuning of a single geometric parameter. For each geometric parameter, the adjusted step size is set as 0.1 mm, and the asymmetric metasurface proposed above (P=0.5 mm) is taken as the reference parameter of Δ=0. In Fig. 6, we discuss three parameters: the cylinder radius R, the cylinder height h_0, and the substrate thickness h_1. The position changes of the resonant frequencies of the two modes are plotted in Fig. 6(d). For these three cases, the resonance frequency moves to the short-wave direction with the increase of the parameter size, and the frequency shift is linear to the variation of parameter. Both modes respond to the changes of the two dimensions of the cylinder. When the radius of cylinder R increases, the frequency shifts of the resonant frequencies of the two modes are almost the same. From Δ=–0.2 mm to Δ=0.2 mm, the resonant frequencies of the two modes change from 39 MHz to 37.2 MHz, respectively. And the line width of both modes increases. For the height of the cylinder h_0, it has almost no effect on the linewidth of the two modes. Compared with Mode 1, the frequency shift of Mode 2 is more significant, reaching 101 MHz.

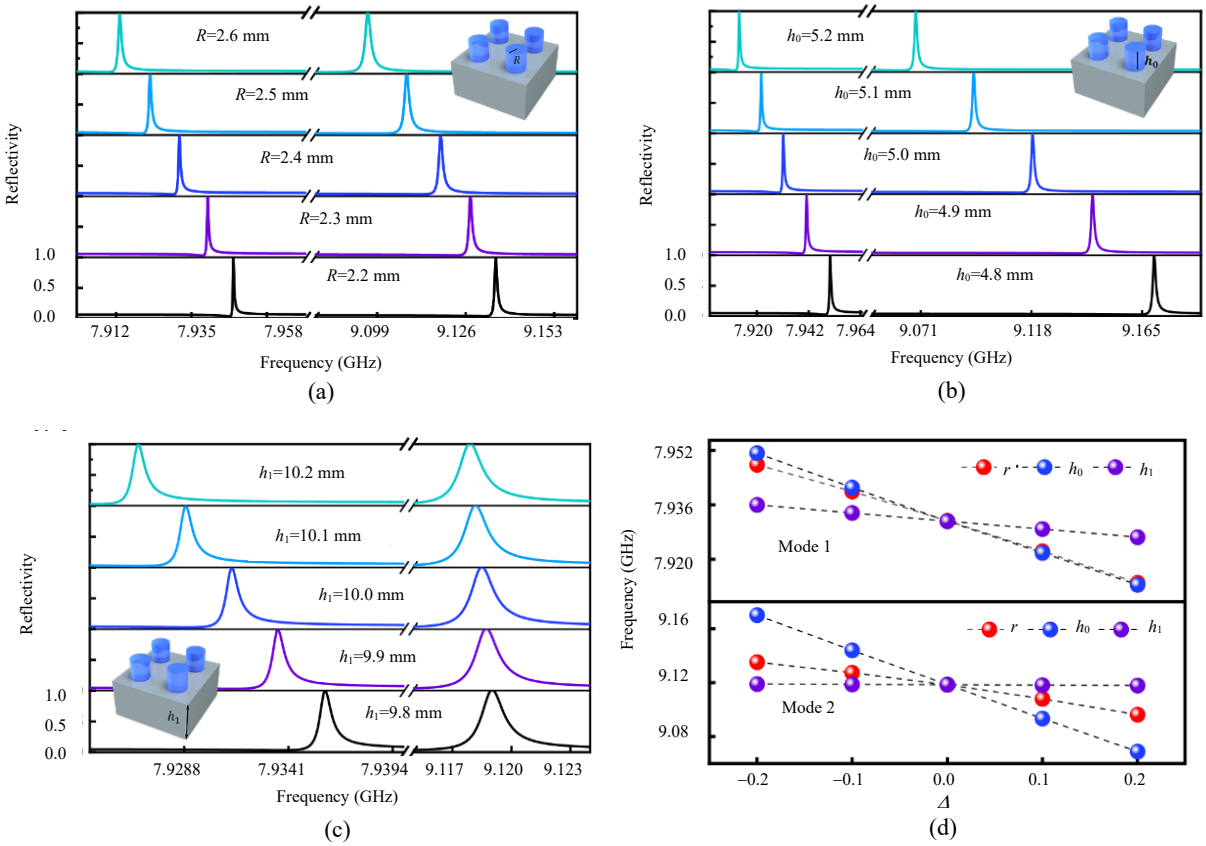

Fig. 6 Reflectance spectra of metasurface with different geometric parameters: (a)–(c) reflectance spectra of metasurface when R, h_0, and h_1 change; (d) resonant frequencies of the two modes varying with geometric parameters.

As shown in Fig. 6(c), with the change of substrate thickness, we can observe that the linewidths of the two resonances do not change, and the resonant frequency of Mode 2 almost does not shift. Although Mode 1 moves slightly in the shortwave direction, the frequency shift is quite small compared to the effect caused by the cylinder size change. This is consistent with our previous assessment. However, it can be seen that the two modes are insensitive to h_1, and the line width of the two modes is unchanged. Mode 1 only has a slight frequency shift, while Mode 2's is almost invisible. In the discussion of the electromagnetic field distribution of the two modes [Fig. 3(c) and 3(e)], it can be observed that the displacement current represented by the black arrow is concentrated on the longitudinal region of the cylinders. The magnetic field vector confined to the substrate range represented by the coloring area in Fig. 3 is the product of the displacement current vortex. In this paper, we mainly reduce the symmetry by changing the position of the cylinders and then transform the symmetry-protected BIC into quasi-BIC, which further indicates that the dual TD resonance are driven by quasi-BIC. In such a structure, the substrate does not materially affect the structure, so the weak effect of the substrate thickness can be expected.

5. Design of GHz ultra-sensitive gas refractive index sensor

The two resonant frequencies of the metasurface are closely related to the refractive index of the background medium, and the asymmetric metasurface has an ultra-high Q factor [21]. These characteristics provide a feasible approach for gas-sensing applications. Based on the asymmetric metasurface mentioned above (P=0.5 mm), we

design an ultra-sensitive gas sensor, and its schematic diagram is shown in Fig. 7(a). We define the distance from the upper surface of the substrate to the upper layer of the detected material as the detection thickness h_2. As h_2 increases, the interaction between the analyte and the electric field becomes stronger, leading to the frequency shift of the resonance. When the thickness of the analyte is higher than that of the fringing electric field, the frequency shift reaches saturation [14]. Therefore, for the stability of the sensor, we set a large enough detection thickness (h_2 =16 mm).

Figure 7(b) indicates the influence of changes in the background refractive index on the two modes. Resonant frequencies of corresponding modes are plotted in Figs. 7(b) and 7(c), and the solid black line represents the linear fitting. Mode 1 shows good linearity to the change of refractive index of the analyte. As the refractive index of the analyte changes from 1.0 to 1.4, Mode 1 is perfectly linear for the refractive index of the analyte, while Mode 2 is linear for the relative permittivity. Moreover, Mode1's FoM and sensitivity are better than Mode 2's, so it is more valuable to use the fluctuation range of Mode 1 resonance as the working frequency band of the sensor.

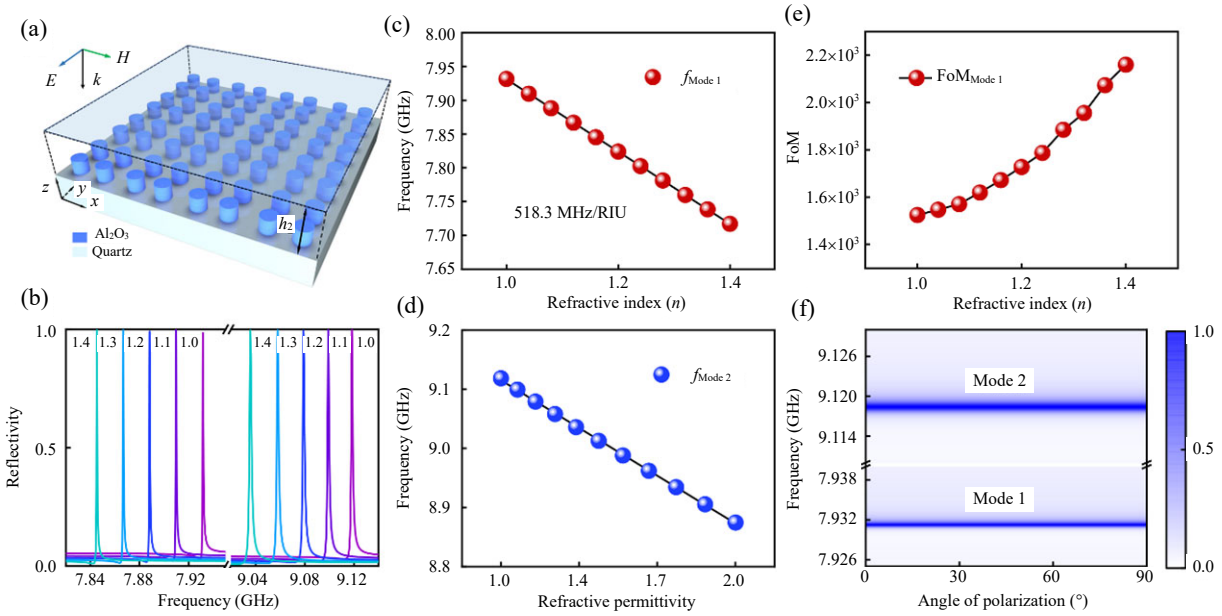

Fig. 7 Metasurface working as ultra-sensitive as refractive index sensor: (a) schematic of GHz ultra-sensitive gas refractive index sensor, (b) reflection spectrum of different refractive index of background medium, (c)–(d) resonant frequencies of the two modes vary with different refractive index of background medium, (e) FoM of modes with different refractive index of background medium, and (f) polarization characteristic of the GHz sensor.

The sensitivity of Mode 1 resonance reaches 518.3 MHz/RIU and the maximum line width is only 0.34 MHz. The resonant frequency of Mode 2 is negatively correlated with the dielectric constant of the analyte. Figure 7(e) calculates the change of FoM with the increase of the refractive index. FoM is defined as FoM=S/FWHM, where S is the sensitivity. When the refractive index ranges from 1.0 to 1.4, the FoM of Mode1 ranges from 1570 to 2 160, which is higher than the FoM and the sensitivity of the previously reported GHz gas refractive index sensors as shown in Table 1.

As shown in Fig. 3(e), the displacement currents show a circular behavior encircling around the center of each cylinder. This ring-like displacement currents' pattern produces four magnetic moments oriented along the z-axis. This indicates that each cylinder in the superlattice responds independently to the polarization of the incident wave. Displacement currents are generated and vortexed

with adjacent cylinders in the direction of polarization. Since the asymmetric metasurface is derived from a symmetric shift along the diagonal of the unit cell, the C_4 symmetry of the system is topological. Therefore, as shown in Fig. 7(f), the sensor shows polarization independence for the normal incident electromagnetic wave, which is beneficial to the practical application of the sensor.

Table 1 Performances of GHz sensors including type of sensing structure and sensitivity of the developed systems.

Reference	Sensing structure	*S* (MHz/RIU)
[22]	Side-polished optical fibers	293
[23]	Side-polished DBR fiber Laser	141.9
[24]	Micro-nano fiber	369.6
[25]	Tapered optical fibers	293
[26]	Dual SRRs	20
[27]	CSRR	55
This work	All-dielectric metasurface	518.3

6. Conclusions

We propose a GHz ultra-sensitive gas refractive index sensor based on a tetramer cylinders metasurface driven by BIC. By shrinking or expanding the cylinders from the center of the simple lattice along the diagonal direction of the tetramer lattice, BIC is converted into quasi-BIC, and the dual-frequency TD resonance with a high Q factor is obtained. Moreover, the resonance frequency and linewidth can be adjusted flexibly by changing its asymmetric parameters. The sensing of the analyte shows that the TD resonance generated by the GHz sensor is perfectly linear to the variation of refractive index and polarization independent. Its sensitivity is 518.3 GHz/RIU and FoM is 2160. The sensitivity is higher than that of the previously proposed GHz sensor, and FoM can be further improved by reducing the asymmetric parameters. And it has the characteristics of simple process and low cost in the millimeter scale. We believe that the proposed structure will be an excellent and stable alternative system for biochemical detection.

Acknowledgment

This work was supported in part by the National Natural Science Foundation of China (Grant No. 11811530052); Intergovernmental Science and Technology Regular Meeting Exchange Project of Ministry of Science and Technology of China (Grant No. CB02-20); Open Fund of State Key Laboratory of Applied Optics (Grant No. SKLAO2020001A04); Undergraduate Research and Innovation Projects of China (Grant No. 2021102Z).

References

[1] C. Wu, N. Arju, G. Kelp, J. A. Fan, J. Dominguez, E. Gonzales, *et al.*, "Spectrally 228 selective chiral silicon metasurfaces based on infrared Fano resonances," *Nature Communications*, 2014, 5(1): 1–9.

[2] I. Al-Naib, C. Jansen, and M. Koch, "High-Q factor metasurfaces based on miniaturized asymmetric single split resonators," *Applied Physics Letters*, 2009, 94(15): 153505.

[3] G. Quaranta, G. Basset, O. J. F. Martin, and B. Gallinet, "Recent advances in resonant waveguide gratings," *Laser & Photonics Reviews*, 2018, 12(9): 1800017.

[4] R. S. Savelev, D. S. Filonov, M. I. Petrov, A. E. Krasnok, P. A. Belov, and Y. S. Kivshar, "Resonant transmission of light in chains of high-index dielectric particles," *Physical Review B*, 2015, 92(15): 155415.

[5] J. Zhong, X. Xu, and Y. S. Lin, "Tunable terahertz metamaterial with electromagnetically induced transparency characteristic for sensing application," *Nanomaterials*, 2021, 11(9): 2195.

[6] B. Min, E. Ostby, V. Sorger, E. Ulin-Avila, L. Yang, X. Zhang, *et al.*, "High-Q surface-plasmon-polariton whispering-gallery microcavity," *Nature*, 2009, 457(7228): 455–458.

[7] D. N. Maksimov, V. S. Gerasimov, S. Romano, and S. P. Polyutov, "Refractive index sensing with optical bound states in the continuum," *Optics Express*, 2020, 28(26): 38907–38916.

[8] S. Romano, G. Zito, S. Torino, G. Calafiore, E. Penzo, G. Coppola, *et al.*, "Label-free sensing of ultralow-weight molecules with all-dielectric metasurfaces supporting bound states in the continuum," *Photonics Research*, 2018, 6(7): 726–733.

[9] F. H. Stillinger and D. R. Herrick, "Bound states in the continuum," *Physical Review A*, 1975, 11(2): 446.

[10] C. W. Hsu, B. Zhen, A. D. Stone, J. D. Joannopoulos, and M. Soljai, "Bound states in the continuum," *Nature Reviews Materials*, 2016, 1(9): 1–13.

[11] K. Koshelev, S. Lepeshov, M. Liu, A. Bogdanov, and Y. Kivshar, "Asymmetric metasurfaces with high-Q resonances governed by bound states in the continuum," *Physical Review Letters*, 2018, 121(19): 193903.

[12] Y. He, G. Guo, T. Feng, Y. Xu, and A. E. Miroshnichenko, "Toroidal dipole bound states in the continuum," *Physical Review B*, 2018, 98(16): 161112.

[13] T. Bai, Q. Li, Y. Wang, Y. Chen, Z. D. Hu, and J. Wang, "Terahertz vortex beam generator based on bound states in the continuum," *Optics Express*, 2021, 29(16): 25270–25279.

[14] Y. Wang, Z. Han, Y. Du, and J. Qin, "Ultrasensitive terahertz sensing with high-Q toroidal dipole resonance governed by bound states in the continuum in all-dielectric metasurface," *Nanophotonics*, 2021, 10(4): 1295–1307.

[15] S. Li, C. Zhou, T. Liu, and S. Xiao, "Symmetry-protected bound states in the continuum supported by all-dielectric metasurfaces," *Physical Review A*, 2019, 100(6): 063803.

[16] Y. Fan, F. Zhang, N. H. Shen, Q. Fu, Z. Wei, H. Li, *et al.*, "Achieving a high-Q response in metamaterialsby manipulating the toroidal excitations," *Physical Review A*, 2018, 97(3): 033816.

[17] Q. Mi, T. Sang, Y. Pei, C. Yang, S. Li, Y. Wang, *et al.*, "High-quality-factor dual-band Fano resonances induced by dual bound states in the continuum using a planar nanohole slab," *Nanoscale Research Letters*, 2021, 16(1): 1–11.

[18] Y. W. Huang, W. T. Chen, P. C. Wu, V. Fedotov, V. Savinov, Y. Z. Ho, *et al.*, "Design of plasmonic toroidal metamaterials at optical frequencies," *Optics Express*, 2012, 20(2): 1760–1768.

[19] S. Han, L. Cong, F. Gao, R. Singh, and H. Yang, "Observation of Fano resonance and classical analog of electromagnetically induced transparency in toroidal metamaterials," *Annalen der Physik*, 2016, 528(5): 352–357.

[20] N. Kazemi, K. Schofield, and P. Musilek, "A high-resolution reflective microwave planar sensor for sensing of vanadium electrolyte," *Sensors*, 2021, 21(11): 3759.

[21] J. F. Algorri, D. C. Zografopoulos, A. Ferraro, B. García-Cámara, R. Vergaz, R. Beccherelli, *et al.*, "Anapole modes in hollow nanocuboid dielectric metasurfaces for refractometric sensing," *Nanomaterials*, 2018, 9(1): 30.

[22] R. Bernini, G. Persichetti, E. Catalano, L. Zeni, and A. Minardo, "Refractive index sensing by Brillouin scattering in side-polished optical fibers," *Optics Letters*, 2018, 43(10): 2280–2283.

[23] X. Yang, S. Bandyopadhyay, L. Y. Shao, D. Xiao, G. Gu, and Z. Song, "Side-polished DBR fiber laser with enhanced sensitivity for axial force and refractive index measurement," *IEEE Photonics Journal*, 2019, 11(3): 1–10.

[24] H. Chenhui, Q. Li, L. Hao, and C. Linghao, "Brillouin refractive index sensing technique based on micro-nano fiber," *Laser & Optoelectronics Progress*, 2019, 56(17): 170626.

[25] A. Minardo, L. Zeni, R. Bernini, E. Catalano, and R. Vallifuoco, "Quasi-distributed refractive index sensing by 267 stimulated Brillouin scattering in tapered optical fibers," *Journal of Lightwave Technology*, 2022, 40(8): 2619–2624.

[26] M. Abdolrazzaghi and M. Daneshmand, "Dual active resonator for dispersion coefficient measurement of asphaltene nano-particles," *IEEE Sensors Journal*, 2017, 17(22): 7248–7256.

[27] Z. Liu, Y. Xu, Y. Lin, J. Xiang, T. Feng, Q. Cao, *et al.*, "High-Q quasibound states in the continuum for nonlinear metasurfaces," *Physical Review Letters*, 2019, 123(25): 253901.